UC Irvine
UC Irvine Previously Published Works

Title

Change Detection Techniques for ERS-1 SAR Data

Permalink

Journal

IEEE Transactions on Geoscience and Remote Sensing, 31(4)

ISSN

0196-2892

Authors

Rignot, EJM

Zyl, JJV

Publication Date

1993

DOI

10.1109/36.239913

Copyright Information

Peer reviewed

Change Detection Techniques for ERS-1 SAR Data

Eric J. M. Rignot, *Member, IEEE,* and Jakob J. van Zyl, *Member, IEEE*

Abstract—Several techniques for detecting temporal changes in satellite synthetic aperture radar (SAR) imagery are compared using both theoretical predictions and spaceborne SAR data collected by the European first Remote Sensing Satellite, ERS-1. In a first set of techniques, changes are detected based on differences in the magnitude of the signal intensity between two dates. Ratioing of the multidate radar intensities is shown to be better adapted to the statistical characteristics of SAR data than subtracting, and works best when the number of looks is large. In a second set of techniques, changes are detected based on estimates of the temporal decorrelation of speckle. This method works best with one-look complex amplitude data, but can also be used with intensity data provided that the number of looks is small. The two techniques, ratioing of the signal intensity and decorrelation of speckle, are compared using actual SAR data collected by ERS-1. The results illustrate the viability as well as the complementary character of these techniques for detecting changes in the structural and dielectric properties of remotely sensed surfaces. Finally, change detection using the ratio method is applied to mosaics of repeat-pass SAR imagery to illustrate the potential of this method for monitoring applications at the regional scale.

I. INTRODUCTION

DETECTING temporal changes in the state of remotely sensed natural surfaces by observing them at different times is one of the most important applications of Earth-orbiting satellite sensors because they can provide multidate digital imagery with consistent image quality, at short intervals, on a global scale, and during complete seasonal cycles. A lot of experience has already been accumulated in exploring change detection techniques for visible and near infrared data collected by Landsat [1]. In the case of spaceborne synthetic aperture radar (SAR) imagery, change detection techniques have been developed for the temporal tracking of multiyear sea-ice floes using Seasat SAR observations [2], and rainfall events have been detected based on spatial radiometric variations in multidate Seasat SAR imagery [3]. Seasat SAR, however, did not provide calibrated radar measurements, and multidate observations were produced in limited quantity due to the short duration of the mission. Change detection techniques for spaceborne SAR data have not yet been fully explored.

With the launch of the European Space Agency (ESA) first Earth Remote Sensing Satellite (ERS-1) in July 1991, the Japanese first Earth Resources Satellite (J-ERS-1) in February 1992, and the Canadian RADARSAT in 1995, multidate SAR data are now generated and archived on a regular basis, at short intervals, over the entire planet, and for many years to come. This new generation of SAR sensors is characterized by an enhanced image quality (in particular a stable and reliable calibration of the data), and a significant increase in data volume, data rates, and duration of the mission. As a consequence, there is an important need for developing automated procedures of change detection for SAR data that can help human interpretors or subsequent computer algorithms analyze the data and relate the observed changes in radar backscatter with changes in the structural and dielectric properties of the remotely sensed areas.

Change detection techniques for SAR data can be divided into several categories, each corresponding to different image quality requirements. In a first category, changes are detected based on the temporal tracking of objects or stable image features of recognizable geometrical shape. Absolute calibration of the data is not required, but the data must be rectified from geometric distortions due to differences in imaging geometry or SAR processing parameters, and the accurate spatial registration of the multidate data is essential. Applications include sea-ice monitoring and motion tracking, monitoring of glaciers, landslides, and oceanic features. In a second category, changes are detected based on temporal differences in radar backscatter. The requirements are a stable calibration accuracy of the data, and an accurate spatial registration of the multidate data. Typical applications include monitoring of crops, volcanic activity, snow extent and conditions, glacial melt, soil moisture, and vegetation water content [4]. Finally, change detection techniques may be applied to data collected by more than just one sensor, for example, combining Seasat SAR data collected in 1978 with J-ERS-1 SAR data collected in 1992.

In this paper, we limit ourselves to the study of SAR-specific change detection techniques based on detecting changes in radar backscatter from land surfaces using repeat-pass imagery. Two sets of techniques adapted to the statistical characteristics of SAR data are presented and compared using both theoretical predictions and actual data collected by ERS-1 SAR. The paper is organized as follows. Section II presents the ERS-1 mission, and summarizes the characteristics of repeat-pass ERS-1 SAR imagery, their calibration, and their registration. Knowledge of these images characteristics strongly influences the selection of candidate change detection techniques. Section III presents change detection techniques based on differencing of the multidate radar intensities. Section IV discusses change detection techniques based on the temporal decorrelation of speckle. Section V shows several examples of change detection applications using ERS-1 SAR, and conclusions are given in Section VI.

II. REPEAT-PASS ERS-1 IMAGERY

ERS-1 currently follows a sun-synchronous orbit with an orbital inclination of 97°, and had a 3-day repeat cycle from August to December 1991 during the commissioning phase, followed by a 35-day repeat cycle during the multidisciplinary phase started in January 1992. ERS-1 operates a SAR instrument at C-band frequency ($\lambda = 5.7$ cm), VV-polarization (that is, vertical transmit and vertical receive polarization), 23° look angle, 100-km swath width, and with a spatial resolution better than 30 m [5]. As ERS-1 does not carry an on-board SAR data recorder, SAR data are only acquired in view of an Earth-based receiving station. The ERS-1 SAR data presented in this paper are from NASA's Alaska SAR Facility (ASF), at the University of Alaska, Fairbanks, AK [6].

During the 1991 commissioning phase, ERS-1 followed very accurate satellite orbits, with a 3-day repeat cycle which for some parts of the world, including Alaska, provided exact repeat coverage every 3 days. Within the ASF receiving station mask, ERS-1 overflew the same areas, at the same time of the day, with the same imaging geometry. The incidence angle of the radar signal onto the remotely sensed area was repeated within fractions of a degree, and the geometric distorsions and radiometric calibration errors introduced in the imagery due to topographic variations were also exactly repeated. Repeat-pass slant-range ERS-1 SAR images are therefore directly usable for change detection and monitoring applications, and there is no need for geometric rectification of the data and for projections and resampling to a common Earth-fixed grid. Registration of multidate repeat-pass slant-range images is a straightforward process limited to the determination of an azimuth shift (due to a different processing start time for the first range line, and slight differences in time of overpass of the satellite between two passes), and a residual slant-range shift (due to differences in SAR processing parameters and slight changes in the trajectory of the satellite), typically about 1 or 2 pixel elements, i.e., 30 m. To determine this pixel offset with subpixel accuracy, we compute the correlation peak of the signal intensity between the two SAR images. This method is reliable even in the presence of large changes in the signal intensity because numerous and stable textural features are always present in the imagery.

Mosaicking of SAR data acquired along the same flight line or transect is more difficult because the data are corrupted by geometric distortions that vary along track due to relative changes in altitude, Earth velocity, and attitude of the ERS-1 satellite. The azimuth pixel spacing is higher in near-range by 0.04% and 0.11% due to differential Earth circumference and velocity, respectively. The slant-range pixel spacing varies between 12.493 and 12.507 m between the first and last record [7]. Since consecutive images along track are processed with slightly different processing parameters, the geometric distortions in their overlapping segments are not identical. Typically, two consecutive images overlap by 134 lines (over a total of 1024 lines), and the correlation peak varies by about ±0.25 pixels in slant-range, as a result of differential geometric distortions. We computed the correlation peak of the signal intensity at midrange as a compromise, but registration errors

are visible at the transition boundary between two scenes. These registration errors are difficult to identify by a human eye from a SAR image display, but they appear distinctly in change detection maps because the process of change detection is sensitive to subpixel registration errors, which are difficult to avoid in mountainous terrain where large transitions in pixel brightness occur within a single pixel and geometric distorsions are important.

One of the most important characteristics of ERS-1 SAR is the stability of its radar gain. The standard error of the radar gain is currently less than 0.4 dB according to ESA's active external calibration devices [8], and in good agreement with the predicted stability of 0.33 dB measured during ground testing [5]. The remarkable stability of ERS-1 radar gain, combined with the great accuracy of its repeat-orbit cycle and its short revisit interval, render ERS-1 repeat-pass SAR imagery very suitable to change detection applications. Since the calibration factors (that is, absolute radar gain, and antenna pattern removal) are already included in the ASF/SAR processor [9], no calibration work was required in this study.

In the next sections, we describe and compare several change detection techniques for ERS-1 repeat-pass SAR data.

III. CHANGE DETECTION USING THE DIFFERENCE

Differencing and ratioing are well-known techniques for change detection [1]. In differencing, changes in radar backscatter are measured by subtracting the intensity values, pixel per pixel, between two dates; in ratioing, changes are measured by dividing the intensity values, pixel per pixel, and are conveniently expressed in decibels (that is, taking ten times the logarithm in base ten of the ratio of the intensities). In this section, the two methods are compared based on their statistics and probability of error.

The multilook SAR intensities are assumed to be gamma distributed as

$$p\left(I_0 / \langle I_0 \rangle\right) = \frac{N^N I_0^{N-1}}{\langle I_0 \rangle^N (N-1)!} \exp\left\{-\frac{N I_0}{\langle I_0 \rangle}\right\} \qquad (1)$$

where $\langle I_0 \rangle$ is the mean intensity of an homogeneous region at time t_0, and N is the equivalent number of looks of the SAR data. Since a premise of change detection is that radar intensities do change between time t_0 and t_1, the intensities I_0 and I_1 acquired, respectively, at times t_0 and t_1 over the same resolution cell are assumed to be mathematically independent. The joint distribution of I_0 and I_1 is therefore the product of their marginal distributions given in (1).

The distribution of the difference ($d = I_1 - I_0$) of the signal intensities is derived after a change in variables by integrating the joint distribution over I_0, leading to [10]

$$p\left(d / \langle I_0 \rangle, \langle I_1 \rangle\right) = \frac{N^N}{(N-1)!} \frac{\exp\left\{-N \frac{d}{\langle I_1 \rangle}\right\}}{(\langle I_1 \rangle + \langle I_0 \rangle)^N}$$
$$\times \sum_{j=0}^{j=N-1} \frac{(N-1+j)!}{j!(N-1-j)!}$$
$$\cdot d^{N-1-j} \left[\frac{\langle I_0 \rangle \langle I_1 \rangle}{N(\langle I_0 \rangle + \langle I_1 \rangle)}\right]^j. \qquad (2)$$

The mean of the difference and the mean of the square difference are

$$E(d) = \frac{\langle I_0 \rangle}{n} \sum_{j=0}^{j=n-1} \frac{(n-j)(n-1+j)!}{j!(n-1)!}$$
$$\cdot \frac{(\langle I_1 \rangle / \langle I_0 \rangle)^{n+1}}{(1 + \langle I_1 \rangle / \langle I_0 \rangle)^{n+j}} \tag{3}$$

$$E(d^2) = \frac{\langle I_0 \rangle \langle I_1 \rangle}{n^2} \sum_{j=0}^{j=n-1} \frac{(n-j+1)(n-j)(n-1+j)!}{j!(n-1)!}$$
$$\cdot \frac{(\langle I_1 \rangle / \langle I_0 \rangle)^{n+1}}{(1 + \langle I_1 \rangle / \langle I_0 \rangle)^{n+j}}$$

where $E(x)$ denotes the expected value of the random variable x. The distribution of the difference given in (2) depends on both the relative change $(\langle I_1 \rangle / \langle I_0 \rangle)$, and on a reference intensity level, i.e., either $\langle I_0 \rangle$ or $\langle I_1 \rangle$. As a consequence, changes will not be detected in the same fashion in high intensity regions compared to low intensity regions, which is not a desired effect. When the intensities $\langle I_0 \rangle$ and $\langle I_1 \rangle$ are multiplied by a constant factor α, (3) shows that both $(E(d))^2$ and $E(d^2)$ are multiplied by α^2, which means that the variance of the distribution of the difference increases with the intensity level. Since the probability of error in detecting changes increases with the variance of the distribution, this result shows that the difference method will produce more errors in the high intensity regions of the image than in the low intensity regions, so that the difference method is not adapted to the statistics of SAR images.

Similarly, the distribution of the ratio ($r = I_1/I_0$) is derived after a change in variables by integrating the joint distribution over I_0 leading to [10]–[12]

$$p\left(r / \langle I_0 \rangle, \langle I_1 \rangle\right) = \frac{(2N-1)!}{(N-1)!^2} \frac{\bar{r}^N r^{N-1}}{(\bar{r} + r)^{2N}} \tag{4}$$

where $\bar{r} = \langle I_1 \rangle / \langle I_0 \rangle$. The mean and standard deviation of the ratio are

$$E(r) = \frac{n}{n-1} \bar{r} \tag{5}$$
$$\sigma(r) = \frac{n(2n-1)\bar{r}}{(n-1)^2(n-2)}.$$

In contrast to the distribution of the difference, the distribution of the ratio given in (4) only depends on the relative change $\bar{r}$ in average intensity between two dates, and detecting changes in the SAR imagery does not depend on the intensity level of the pixels. To evaluate in a more quantitative fashion the error produced by the ratio method, we now compute its probability of error as a function of the change in radar intensity between two dates.

If we assume a threshold r_0 to decide on whether to classify a given change in radar backscatter between class A characterized by a change $r_A = \langle I_A \rangle / \langle I_0 \rangle$ or class B characterized by a change $r_B = \langle I_B \rangle / \langle I_0 \rangle$ (i.e., $r > r_0$ is classified as class B, and $r \leq r_0$ is classified as class A, and assuming $r_B > r_A$), the class A probability of error is given by
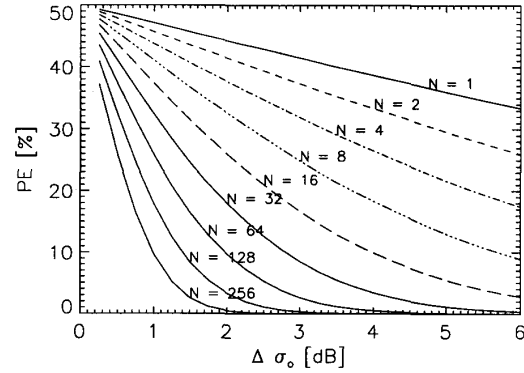
$$PE_A = \int_{r_0}^{\infty} p(r/r_A) dr \tag{6}$$

Fig 1. Probability of error (in %) of the ratio method versus the change in radar backscatter $\Delta\sigma_0$ (in decibels) between the two dates, for a number of looks N varying between 1 and 256.

and the class B probability of error by

$$PE_B = \int_0^{r_0} p(r/r_B) dr. \tag{7}$$

Assuming equal *a priori* probabilities for classes A and B, the threshold decision is found using

$$p(r_0/r_A) = p(r_0/r_B) \tag{8}$$

leading to

$$r_0 = \sqrt{r_A r_B} \tag{9}$$

which is independent of the number of looks N. The total probability of error is

$$PE = \frac{1}{2}(PE_A + PE_B) \tag{10}$$

which is found to be equal to

$$PE = 1/2 - f(X) + f(1/X) \tag{11}$$

where

$$f(X) = \frac{X^N}{2(N-1)!(1+X)^{2N-1}}$$
$$\cdot \left[\sum_{j=0}^{j=N-1} \frac{(2N-j-2)!}{(N-j-1)!}(1+X)^j \right] \tag{12}$$

and $X = \sqrt{r_B/r_A}$. A plot of PE as a function of the change in radar backscatter intensity, $\Delta\sigma^0 = 20\log_{10}(X)$, expressed in decibels, is shown in Fig. 1 for different values of N. The results show that PE decreases slowly with an increasing number of looks N. To detect changes in radar intensity less than 2 dB with a confidence level better than 90% (that is PE = 10 %), N must be greater than 64 looks, which means a large number of independent SAR samples. Detecting changes in radar backscatter of the order of one decibel requires a number of looks larger than a hundred. Hence, the ratio method is quite sensitive to the presence of image speckle in the sense that speckle patterns that are difficult to detect by a human eye in SAR images when the number of looks is large will still be visible in ratio images.

Another important reason for selecting the ratio method instead of the difference method is that the ratio method is very robust to calibration errors whereas the difference method is not. Radiometric errors are usually introduced in the imagery during SAR processing by assuming a flat Earth model, resulting in two errors: 1) an error in the computation of the scattering element size due to errors in the true incidence angle of the electromagnetic signal onto the surface; and 2) an error in the antenna pattern removal due to errors in the true depression angle of the signal onto the reflecting surface [13]. Both errors are multiplicative factors to the total radar intensity. These factors are eliminated when computing the ratio image because calibration errors are exactly reproduced in repeat-pass imagery. In contrast, in the difference method, radiometric errors directly modulate the difference of the radar intensities, typically yielding higher changes in very hilly terrain (e.g., slopes facing the radar) than in rather flat areas for the same type of surface, which is not a desired effect.

In most applications, it is necessary to threshold the ratio image to identify image pixels that change by more than $\pm x$ dB, where x is a real number. Selecting threshold values depends on the application and on the nature and magnitude of the expected changes, and can generally be viewed as an optimization problem with a number of constraints. We will not address this topic in this paper. Given threshold values, image pixels are classified into classes, each of which corresponds to a well defined change in magnitude of the radar intensity. Equation (9) shows that an optimum threshold for classifying a pixel into class A or class B is given in decibels by $T = \frac{1}{2}(10\log_{10}(r_A) + 10\log_{10}(r_B))$, independent of the number of looks N, because this operation corresponds to a maximum likelihood classification of the ratio image into a number of classes of changes. To improve the results, one possibility is to include the *a priori* probabilities of the classes in the classification process and perform a maximum *a posteriori* classification of the data. An example of maximum *a posteriori* (MAP) classifier for change detection applications was proposed in [12]. The *a priori* distribution of the classes is modeled using a Markov random field, and is combined with the *a priori* distribution of the ratios (4) to yield an expression for the *a posteriori* distribution of the classes given the ratios over the entire image array. Bayes' optimal classification of the ratio image maximizes the *a posteriori* distribution of the classes over the entire scene. Although the exact solution to this optimization problem is extremely difficult to compute, approximate solutions can be obtained. Several techniques are possible, depending on computational cost versus quality of the solution, as discussed in [12], [14]. An example of MAP classification using ERS-1 SAR data is given in Section V.

Other techniques have been proposed to detect changes in digital satellite imagery, including multidate classification of the data, and principal component analysis [1]. Results obtained with Landsat data indicate that these more sophisticated techniques do not perform better than a simple differencing of the images. We did not test them on SAR data. In the next section, we will present a novel SAR-specific change detection technique based on the temporal decorrelation of speckle. In principle, temporal decorrelation of speckle may arise even

when no changes in the radar intensity are detected, so that this change detection technique may detect small changes in radar backscatter that could not be detected using the ratio because of limitations imposed by image speckle (Fig. 1) or by the radar gain stability.

IV. CHANGE DETECTION USING THE DECORRELATION OF SPECKLE

According to the random walk model of speckle [15], decorrelation of speckle may arise from a redistribution of the scatterers within a resolution cell, either as a result of random displacements of the scatterers due to external disturbances, or because the scatterers change totally in nature and distribution between the two dates. Hence, the temporal decorrelation of speckle provides information about possible changes in the surface structural and dielectric properties. The detected changes are independent of the calibration accuracy of the data.

The decorrelation of speckle is not measured directly by SAR, because there are other sources of signal decorrelation in repeat-pass SAR imagery. These sources are: 1) a decorrelation due to thermal noise; 2) a spatial baseline decorrelation; and 3) a temporal decorrelation of speckle [16] . The total correlation coefficient is modeled as the product of the correlation coefficients from these independent sources of decorrelation as

$$\rho_a = \rho_n \, \rho_B \, \rho_s \qquad (13)$$

where

$$\rho_n = \frac{1}{1 + \text{SNR}^{-1}}; \quad \rho_B = 1 - \frac{2 \mid B \mid R_y \cos^2\theta}{\lambda R}. \qquad (14)$$

SNR is the signal-to-noise ratio, B is the antenna baseline separation (assumed to be in the horizontal direction), R_y is the spatial resolution in azimuth, θ is the look angle, λ is the radar wavelength, R is the range distance to the radar, ρ_a is the magnitude correlation coefficient of the SAR complex amplitudes (that is, amplitudes and phases of the signal expressed as complex numbers), ρ_n is the thermal noise decorrelation coefficient, ρ_B is the spatial baseline decorrelation coefficient, and ρ_s is the temporal decorrelation of speckle. Knowing the thermal noise power level, and the antenna baseline separation between repeat-passes, one can estimate ρ_s from ρ_a. In the case of ERS-1 SAR, $R_y = 30$ m, $\lambda = 5.7$ cm, $\theta = 23°$, and $R = 830$ km so that the effect of the spatial baseline decorrelation is significant when $B \geq 460$ m (that is, $\rho_B \leq 0.5$). The effect of thermal noise is significant for SNR$\leq$ 1 dB (for which $\rho_n \leq 0.6$), which means radar intensities close to the system noise floor. Equation (14) shows that ρ_B does not vary significantly within a SAR scene, because R and $\cos(\theta)$ vary by 10% and 5% across swath, respectively, and R_y and λ are constant. Hence, if a large value of ρ_a is detected in an area of large SNR, that value will set a lower limit on ρ_B, and practically insure that the effect of the spatial baseline decorrelation can be ignored in the analysis of spatial changes in ρ_a.

We estimate the temporal decorrelation of the signal using

$$\rho_a = \left| \frac{\langle a_0 \, a_1^* \rangle}{\sqrt{\langle |\, a_0 \,|^2 \rangle \langle |\, a_1 \,|^2 \rangle}} \right| \tag{15}$$

where a_0 and a_1 are the SAR complex amplitudes measured, respectively, at time t_0 and t_1. A large number of samples is required to obtain an accurate estimate of ρ_a because of speckle. When speckle is highly correlated between the two dates, the variance to mean square ratio of the estimate of the spatial correlation of one-look complex amplitudes is given in [14]. In this study, we used one-look SAR complex data, 4096 pixels in range by 12 000 pixels in azimuth, and added the different terms required to estimate the local averages in Equation (15) by taking 4 pixels in range and 20 pixels in azimuth to obtain an 80-looks image of ρ_a that is 512 pixels by 600 pixels in size with nearly square pixels. As neighboring pixel samples are not rigorously independent because pixel spacing is usually selected equal to half the width of the radar impulse response, the effective number of looks N is only 55 when estimated correctly using the equation

$$N = \frac{N_z^2 \, N_r^2}{\sum_{i=0}^{i=N_z-1} \sum_{j=0}^{j=N_r-1} |\, \rho_{a_0}(i,j) \,|^2} \tag{16}$$

where N_z and N_r are, respectively, the number of pixel samples in azimuth and in range, $\rho_{a_0}(i,j)$ is the spatial correlation coefficient of the single-look complex data acquired at time t_0, i is the displacement in pixel in azimuth, and j is the displacement in pixel in range. When $N = 55$, the variance to mean square ratio of ρ_a varies between 13% for $|\, \rho_a \,| = 0.2$ and 2% for $|\, \rho_a \,| = 0.9$, which is reasonably low. Note that ρ_a is independent of spatial variations in radar backscatter cross-section of the surface as discussed in [14].

Disadvantages of the decorrelation technique are the volume of data to be manipulated, the computational cost, and the difficulty to generate one-look complex amplitude SAR data products for a large community of users as these data are intermediate products that are not saved after SAR processing. An alternative is to consider the decorrelation of the signal intensity $I = |\, a \,|^2$ between two dates. The correlation coefficient of the intensity, noted ρ_I, is estimated using

$$\rho_I = \frac{\langle I_0 \, I_1 \rangle - \langle I_0 \rangle \langle I_1 \rangle}{\sqrt{\langle I_0^2 - \langle I_0 \rangle^2 \rangle} \, \sqrt{\langle I_1^2 - \langle I_1 \rangle^2 \rangle}}. \tag{17}$$

The phase of the radar return is not used. In the absence of a textural modulation of the SAR signal due to the natural spatial variability of the radar backscatter cross section of the reflecting surface

$$\rho_I = |\, \rho_a \,|^2 \tag{18}$$

using a fundamental property of circular symmetric Gaussian processes. Equation (18) shows that taking the square root of ρ_I yields an estimate of $|\, \rho_a \,|$. This equality does not hold, however, if textural variations of the radar backscatter from the surface are present and the number of looks is much larger than one. This effect is explained using a simple multiplicative model of the SAR intensity

$$I_i = \langle I_i \rangle \, T_i \, S_i, i \in \{0, 1\} \tag{19}$$

Day of September	18	19	20	21	22	23	24	25	26
Precipitation (mm)	3	4	0	1	0	0	0	10	0
T_{MAX} (°C)	12	12	13	14	13	13	13	10	10
T_{MIN} (°C)	8	5	5	5	8	9	8	7	6

where T_i is a normalized ($\langle T_i \rangle = 1$) texture random variable that modulates the mean intensity return $\langle I_i \rangle$ of an homogeneous area at time t_i, and S_i is a normalized ($\langle S_i \rangle = 1$) speckle random variable with a mean squared to variance ratio equal to the equivalent number of looks N of the data. Using (18) and (19), we obtain

$$\rho_I = \frac{|\, \rho_a \,|^2 \, (1 + \rho_T \, \sigma_T^2) + N \, \rho_T \, \sigma_T^2}{[1 + (N+1)\sigma_T^2]} \tag{20}$$

assuming that T_0 and T_1 have the same variance σ_T^2. When texture is not present, σ_T^2 is zero, and $\rho_I = |\, \rho_a \,|^2$. When texture is present, and the number of looks N is very large, $\rho_I = \rho_T$, and texture dominates the correlation of the signal, which is not surprising since image speckle is not a dominant source of spatial variability of the signal for large N. As a consequence, the temporal decorrelation of speckle from intensity data can only be detected for N small, in practice with N less than 4. Examples are shown in the next section.

V. EXAMPLES USING ERS-1 SAR DATA

Several examples are shown in this section using multidate data from ERS-1 SAR. The objective here is not to interpret physically the observed changes in radar backscatter but to illustrate the use of change detection techniques with actual spaceborne SAR data. Understanding the reasons for detected changes is a topic of ongoing research.

Fig. 2(a) shows a SAR intensity image acquired by ERS-1 at a center location of 58.4°N, and 155.0°W, within the Katmai National Park and Preserve, Alaska, on September 20, 1991 at 21:26 GMT (that is, 1:26 pm Alaska daylight time), Rev. # (revolution number) 943. The north direction is to the bottom in the figure, with ERS-1 flying from bottom to top (descending pass), looking to its right. The same 50 km by 50 km scene was imaged six days later on September 26, 1991 (Rev. # 1029), at the same time of the day. Weather data collected at King Salmon Airport (58.4°N, 156.4°W, 20 m elevation), 81 km west of the center of the scene, are shown in Table I. Air temperatures did not change significantly between the two dates and remained at about +9°C. Rain occurred one day prior to the imaging of the first scene, and one day prior to the imaging of the second scene. Extrapolation of these weather conditions indicate that air temperatures were probably below zero in mountainous areas above 900 m based on a dry lapse adiabatic rate of 1°C/100 m, and local rain storms probably covered the mountain tops with snow. We do not have weather data and surface observations within the scene itself.

An image of the magnitude of the complex correlation coefficient ρ_a is shown in Fig. 2(d) overlaid on the SAR image.

(a)

(b)

(c)

(d)

Fig. 2. ERS-1 SAR scene acquired near Mount Katmai, Alaska, at a center location of 58.4°N, and 155.0°W. The image is 50 km by 50 km in size. The north direction is to the bottom in the figure, with ERS-1 flying from bottom to top (descending pass), looking to its right. From left to right, starting from the top: (a) Amplitude image (80-look) acquired on September 20, 1991 (Rev. ♯ 943), © ESA, 1991; (b) Correlation coefficient $\sqrt{\rho_I}$ of one-look intensity data between 0 and 1; (c) Ratio image $\Delta\sigma_0$ between -2 and +2 dB; (d) Correlation coefficient ρ_a of one-look complex amplitude data between 0 and 1. (b)–(d) are overlaid on the SAR image, which means that the amplitude of the SAR signal is used as a saturation factor between 0.5 and 1.0 on the red, blue, and green channels.

We overlaid the results of the change detection algorithms on the SAR data because topographic variations are totally eliminated in the change detection maps as predicted from the near perfect repeat-pass of ERS-1 over the same areas, and areas of change are difficult to position in the SAR imagery by a human interpreter without identifiable reference points. To construct this data overlay, we modulated the saturation of the red, green, and blue channels by a factor between 0.5 and 1., depending on the magnitude of the SAR signal. In many

areas of Fig. 2(d), speckle is highly correlated between the two dates. The maximum value of ρ_a is 0.964 in an area of high SNR, indicating that $\rho_B \geq 0.964$ and does not significantly modulate the results. Low values of ρ_a are seen in valley bottoms in the lower right portion of the figure, and in nearly all mountain tops which include active volcanoes. Correlation of speckle decreases markedly above a certain altitude, perhaps revealing the contours of the tree line, of the snow line, or both. The ratio image shown in Fig. 2(c) reveals changes in

TABLE II
PRECIPITATION RATES AND AIR TEMPERATURES
(MINIMUM-MAXIMUM) RECORDED AT TALKEETNA AIRPORT
(68.18°N, -150.06°W, 108 m elev.) BETWEEN 09/03 AND 09/11

Day of September	3	4	5	6	7	8	9	10	11
Precipitation (mm)	0	1	1	4	3	24	14	4	1
T_{MAX} (°C)	16	18	16	13	13	11	10	16	14
T_{MIN} (°C)	0	6	3	-2	6	3	3	6	4

radar backscatter larger than 2 dB in mountain tops and valley bottoms. In general, changes in σ_0 are detected in areas where ρ_a is low; and, no changes in σ_0 are found where ρ_a is high. Both methods reveal important changes in the physical and electrical properties of the surface at the higher elevations, yet the decorrelation of speckle detects changes in the lower right portion of the figure that cannot be identified in the ratio image. The correlation of speckle computed using one-look SAR intensity data and 4 pixels in range by 20 pixels in azimuth, is shown in Fig. 2(b), revealing a good correspondence between $\sqrt{\rho_I}$ and ρ_a, although the contrast between regions is better in Fig. 2(b). Image features such as ridge tops and slopes facing the radar yield erroneously large values of $\sqrt{\rho_I}$ in Fig. 2(b), because of texture.

Another example is shown in Fig. 3(a) with a scene acquired acquired at the foot of Mount McKinley, at a center location of 62.7° N and −150.3° W. The Iokotsina glacier (upper left corner in the figure) and the Ruth glacier (top center in the figure) are identified with small arrows in the figure. This image was acquired during an ascending pass of ERS-1 (which is also a night-time pass) on September 5, 1991 (Rev. # 720). The north direction is to the top in the figure, with ERS-1 flying from bottom to top, looking to its right. The same scene was imaged 6 days later on September 11, 1991 (Rev. # 806). Weather data collected at Talkeetna Airport, (62.18° N, -150.06°W, 108 m altitude), 62 km south of the center of the 50 km by 50 km scene, indicate precipitation events between the times of imaging of the two scenes, and no precipitation prior to the imaging of the first scene (Table II). Air temperatures at night remained close to 0°C the whole period, suggesting freezing conditions at elevations higher than 200 m. Air-temperatures during the day were warmer at Talkeetna Airport, but probably below 0°C above 1200 m. The higher portions of the glaciers seen in the top part of Fig. 3(a) are at elevations higher than 2000 m.

The complex correlation map shown in Fig. 3(d) indicate a large correlation of speckle between the two dates, even at the higher elevations. Correlation of speckle is low over the glaciers. Random motion of scatterers within one resolution cell results in a complete decorrelation of speckle after rms motion of 2–3 cm at C-band [16]. However, glacier motion may more likely result in a nearly uniform translation of all scatterers within a resolution cell instead, which would result in total decorrelation if the displacements are of the order of one resolution cell or 30 m. Glaciers do not move at such high rates in this region, and the decorrelation of speckle is probably due to changes in their surface physical and electrical properties. This is confirmed by examining the changes in radar backscatter over these same areas. The ratio image shown

in Fig. 3(c) indicates a large increase in radar backscatter over the glaciers and mountain tops. The correlation coefficient of speckle computed from one-look intensity data is shown in Fig. 3(b), and is in good agreement with the results shown in Fig. 3(d), indicating that the decorrelation of speckle can be studied using one-look intensity data. Fig. 3(e) shows an image of the decorrelation of speckle computed using 4-look intensity SAR data. The effect of texture is more pronounced, and the contrast between regions where speckle is correlated and those where speckle is decorrelated is reduced. Yet, areas where speckle is highly correlated are still visible, illustrating that 4-look intensity data can provide information about the degree of correlation of speckle. This result is of interest to SAR interferometry studies because it shows that multilook SAR intensity data could be used to select image pairs for which speckle is highly correlated and interferometric mapping is possible, before correlating and analyzing one-look SAR complex amplitude data, thereby offering a large data volume reduction in processing of the data.

In principle, when the structural and dielectric properties of the reflecting surface change, the correlation of speckle decreases, and the intensity of the radar returns changes. As mentioned earlier, there can also be areas where speckle decorrelates, yet no change in radar backscatter is detected by the SAR system. As an example of practical situation, a forest under varying wind conditions could undergo no change in radar intensity if the soil and vegetation moisture conditions are unchanged, yet temporal decorrelation of speckle could arise from a random motion of branches which efficiently scatter the radar signals at C-band frequency. Surprisingly, we also detected areas where speckle is highly correlated but the radar intensity changes by several decibels. One such area is identified in Fig. 3(a) with a white circle, with changes in radar backscatter larger than 2 dB and a correlation coefficient ρ_a larger than 0.8. A close inspection of both Figs. 3 and 4 reveal that other areas exist where a significant change in radar backscatter is detected and yet ρ_a is greater than 0.5 (height information can still be retrieved when $\rho_a \approx 0.5$ according to [16]). A value of ρ_a greater than 0.8 suggests that the distribution of scatterers within each resolution cell has not changed, while a 2 dB change in radar backscatter indicates that the scattering properties of the scatterers have been modified. We do not have surface observations within those areas to help propose a definite explanation. One practical surface that could result in such scattering properties could be a recently burned forest. Scattering is there dominated by tree-trunk/ground interactions (the branches have been burnt), and a change in the ground moisture conditions and/or in the tree-trunk water content would change the magnitude of the radar returns without any detectable change in the distributions of the scatterers (i.e., the tree trunks), hence resulting in highly correlated speckle.

These first examples illustrate the practicality of ERS-1 repeat-pass SAR data for change detection applications, and demonstrate that numerous changes in the surface structural and electrical properties can be detected using the ratio method or the method based on the decorrelation of speckle. Comparison of these different change detection techniques

(a)   (b)

(c)   (d)

Fig. 3.   ERS-1 SAR scene acquired near Mount McKinley, Alaska, at a center location of 63.4°N, and -150.3°W. The image is 50 km by 50 km in size. The upper left arrow locates the Iokotsina glacier, and the other arrow locates the Ruth glacier. The north direction is to the top in the figure, with ERS-1 flying from bottom to top (ascending pass), looking to its right. From left to right, starting from top (a) Amplitude image (80-looks) acquired on September 5, 1991 (Rev. # 720), © ESA, 1991; (b) Correlation coefficient $\sqrt{\rho_I}$ of one-look intensity data between 0 and 1; (c) Ratio image $\Delta\sigma_0$ between -2 and +2 dB; (d) Correlation coefficient ρ_a of one-look complex amplitude data between 0 and 1; (b) through (e) are overlaid on the SAR amplitude image. A white circle on (c) highlights an area where $\rho_a \approx 0.8$ and $\Delta\sigma_0 \geq 2$ dB. *(Continued on next page.)*

reveals that they do not necessarily reveal the same type of changes in the surface properties under the same environment, illustrating their complementary character. The decorrelation method indicates whether the position of the scatterers has been altered or totally changed from one day to another, but provides no indication on the magnitude of the corresponding change in radar backscatter. In contrast, the ratio method directly measures the magnitude of the change in radar backscatter but does not provide information about possible changes in the nature of the scatterers and is limited by image speckle and the stability of the radar gain. The two techniques complete each other and help reduce the number of possibilities of physical interpretation of the observed changes.
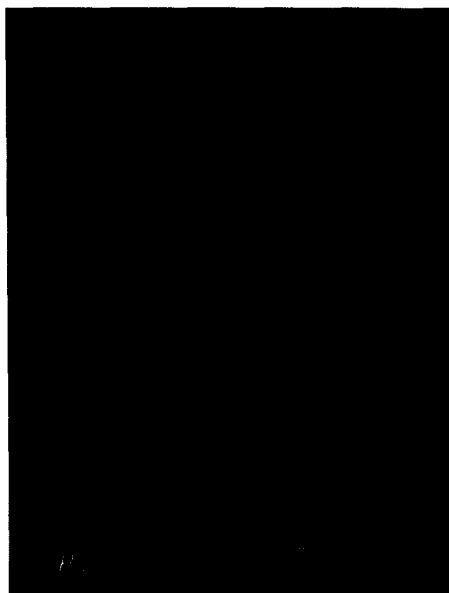
(e)

Fig. 3. *(Continued.)* (e) Correlation coefficient $\sqrt{\rho_I}$ of 4-look intensity data between 0 and 1.

In the next two examples, we examine larger changes in the surface structural and electrical properties detected using the ratio method. We did not analyze the decorrelation of speckle in these examples because image speckle is not expected to remain correlated in areas of large changes separated by several weeks.

Figs. 4(a) and (b) show intensity images acquired by ERS-1 SAR over the Bonanza Creek Experimental Forest (BCEF), near Fairbanks, AK, at a center location of 64.8°N and 147.9°W, respectively, on April 25, 1992 (Rev. # 4067), and on May 30, 1992 (Rev. # 4568). These data are separated by 35 days and were acquired during the 35-day repeat-cycle multidisciplinary phase of ERS-1 during a descending pass of ERS-1 at about 1:00 pm Alaska daylight time. The north direction is to the bottom in the figure, with ERS-1 flying from bottom to top, looking to its right. The scene comprises a mixture of various types of tree species intermixed with treeless areas of short vegetation of shrubs and sedges on a moss layer (see [17] for more details). The Tanana River is visible going across the center of the scene from east to west, corresponding to low pixel brightness values. Weather data collected at this site by the people from the Institute of Northern Forestry in Fairbanks, Alaska, reveal air temperatures of about +4.8°C during the day, and −8.5°C at night, and a soil in the process of thawing ($T_{soil} = -0.1$°C during the day) on Apr. 25, 1992. Air-temperatures were warm ($T = +19.0$°C) with thawed soil ($T_{soil} = +1.0$°C during the day and above zero at night) on May 30, 1992. Changes in radar backscatter larger than 6 dB are detected in the imagery. The color coded ratio image shown in Fig. 4(c) shows areas where the radar backscatter increased by more than 3 dB (yellow), decreased by 3 dB (red), or did not change by more

than 3 dB (blue), overlaid on the SAR image acquired in April. Comparison of the observed changes in radar backscatter with vegetation types reveals that areas colored yellow in Fig. 4(c) are treeless areas (apart from a few points along the river), areas colored red correspond to the river (the disappearance of the rough water ice probably caused the observed decrease in radar backscatter values) and in smaller areas of standing water, and areas colored blue are the forests. For reasons explained earlier on in this paper, the color ratio image shown in Fig. 4(c) is also a maximum likelihood classification map of the area into three classes of changes since the color coding is reduced to three colors only. Fig. 4(d) is an illustration of subsequent improvements in classification quality that can be obtained using a maximum *a posteriori* classifier [12]. The ratio image was classified into three classes of change ($\Delta\sigma_0 \geq +3$ dB, $\Delta\sigma_0 \leq -3$ dB, and $|\Delta\sigma_0| < 3$ dB), and the results are using the same color coding as in Fig. 4(c). The different areas outlined in Fig. 4(c) are better defined in Fig. 4(d). This result indicates that a maximum *a posteriori* classifier provides a worthwhile improvement in segmentation quality for change detection applications compared to a simple thresholding of the ratioed data, which is consistent with the fact that ratio images are very sensitive to image speckle.

Finally, the last example illustrates the potential of the ratio method for detecting changes in radar backscatter at the regional scale. We mosaicked together three SAR images collected during a descending pass of ERS-1 that intercepted with the city of Tanana, 200 km west of Fairbanks, AK. One transect was acquired on September 29, 1991 (Rev. # 1072), while the other was acquired 18 days later, on October 17, 1991 (Rev. # 1330). The mosaic shown in Fig. 5(a) is 100 km by 400 km in size. The north direction is to the top, with ERS-1 flying from top to bottom, looking to its right. As in the previous cases, radiometric distortions due to topography are exactly eliminated in the ratio image, due to the good registration of the data, and the exact repeat-pass of ERS-1 SAR (a small radiometric modulation of the ratio image was introduced using the amplitude data from one of the SAR transect to help reference areas of change in the radar imagery, and are not due to registration errors, as in all the examples shown in this paper). Air temperatures recorded at Tanana Airport (located in the top portion of the figure at 65°.0N and 151°.2W) during that period went from +5°C to −9°C. Similar values were reported at Lake Minchumina Airport (located at 63.54°N, 152.16°C, 213-m elevation). These changes in radar backscatter have been interpreted as resulting from a decrease in the dielectric constant of the soil and vegetation with freezing, which results in a decrease in radar backscatter of the soil and vegetation of approximately 3 dB, nearly independent of landscape, except for areas of standing water (where radar backscatter values may either increase or decrease), and areas that are already in frozen conditions such as high mountain tops where subzero air-temperatures are recorded much earlier in the season [18], [19]. Areas colored red in the ratio image shown in Fig. 5(b) correspond to areas where the landscape (i.e., the soil and vegetation as a single medium) is frozen, whereas areas colored blue froze earlier (case of the mountain range present
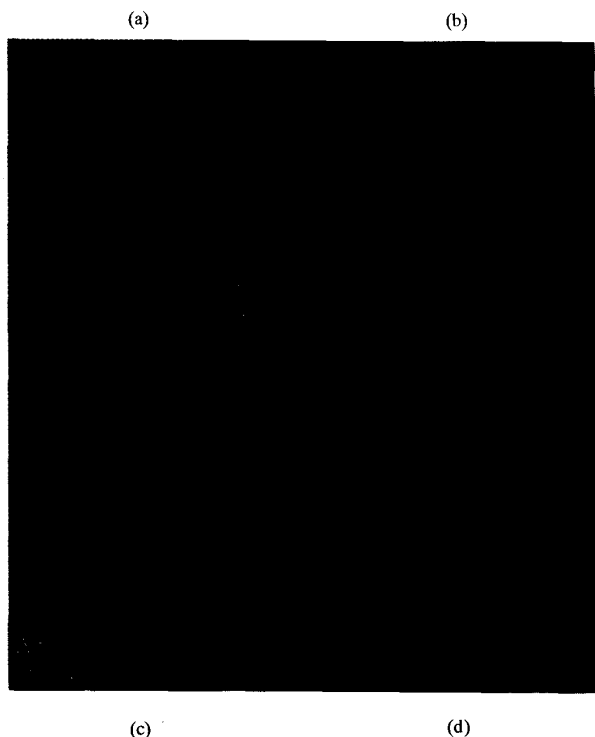
(a) (b)

(c) (d)

Fig. 4. (a) ERS-1 SAR image of the Bonanza Creek Experimental Forest at a center location of 64.8°N and 147.9°W acquired on April 25, 1992 during the 35-day repeat cycle. The image is 19.2 km by 19.2 km in size. The north direction is to the bottom in the figure, with ERS-1 flying from bottom to top, looking to its right, © ESA 1992. (b) ERS-1 SAR image of the same area acquired 35 days later on May 30, 1992, © ESA 1992. (c) Ratio image $\Delta\sigma_0$ between -6 and +6 dB, overlaid on the SAR amplitude data of Fig. 4(a). (d) Classification map of the ratio image of Fig. 4(c) using a maximum *a posteriori* classifier. Pixels colored yellow correspond to $\Delta\sigma_0 \geq +3$ dB, pixels colored red correspond to $\Delta\sigma_0 \leq -3$ dB, and pixels colored blue correspond to $| \Delta\sigma_0 < 3 \text{ dB} |$. The classification map is overlaid on the SAR amplitude data of Fig. 4(a). The saturation factor for the SAR overlay is between 0.5 and 1.2.

(a) (b)

Fig. 5. Mosaic of three ERS-1 SAR images acquired near the city of Tanana, AK (65.10°N and -152.06°W), during the ERS-1 commissioning phase. Each image mosaic is approximately 100 km by 400 km in size. The north direction is to the top in the figure, with ERS-1 flying from top to bottom, looking to its right. (a) Transect acquired on September 29, 1991 (Rev # 1072) during a descending pass of ERS-1 © ESA 1991. (b) Ratio of the SAR intensities measured between September 29, 1991 (Rev. # 1072) and October 17, 1991 (Rev. # 1330) between -4 and +4 dB, and overlaid on the SAR amplitude data.

in the upper portion of the image in Fig. 5(a)), or did not freeze (case of the areas in the lower portion of the image in Fig. 5(a)) because air temperatures were not cold enough yet to yield a complete freezing of the soil and vegetation. The radar backscatter from the Tanana River and Lake Minchumina increased with freezing because of the formation of a rough ice/water interface with freezing.

VI. CONCLUSIONS

Several techniques for change detection have been presented and compared based on their probability of error and on results obtained using repeat-pass ERS-1 SAR data. The method based on the temporal decorrelation of speckle works best with one-look SAR complex amplitude data, but can also be used with multilook intensity data provided that the number of looks is small. Ratioing of the radar intensities works best with multilook intensity data. Areas of change identified by both methods under the same environment do not always agree. For instance, speckle may remain highly correlated although significant changes in radar backscatter

are detected. The decorrelation method helps detects changes in the position of the scatterers whereas the ratio method provides information about the magnitude of the observed changes. Both methods combined enhance our characterization of the observed changes. For instance, if we know that the position of the scatterers is unchanged, then any change in radar backscatter will be related to changes in the electrical properties of the surface and not its structure. Indeed, if both position and scattering properties of the scatterers change, the interpretation is more difficult, but the large complementarity of these two techniques justifies that both of them should be used in detailed monitoring studies. The initial results shown

in this paper illustrate the great potential of ERS-1 for change detection applications. Much work remains to be done to interpret the observed changes in terms of changes of specific parameters controlling the structure and dielectric properties of the landscape, such as surface roughness, biomass, soil and vegetation moisture conditions, or snow depth and water equivalent to mention a few. Although the radar backscatter from natural surfaces depends on all these parameters, plus topography, it is also clear that under certain environmental conditions and over certain time scales, several of these variables may change slowly with time, if at all, so that temporal changes in radar backscatter could be directly related to changes in only one or two parameters. An example is the monitoring of freeze-thaw transitions along north–south Alaskan transects using ERS-1 SAR data, independent of topography and vegetation types [19].

ACKNOWLEDGMENT

REFERENCES

[1] A. Singh, "Digital change detection techniques using remotely sensed data," Int. J. Remote Sensing, vol. 10, pp. 989–1003, 1989.

[2] M. Fily and D. Rothrock, "Sea-ice tracking by nested correlations," IEEE Trans. Geosci. Remote Sensing, vol. GE-25, pp. 570–580, 1987.

[3] F. Ulaby, B. Brisco, and C. Dobson, "Improved spatial mapping of rainfall events with spaceborne SAR imagery," IEEE Trans. Geosci. Remote Sensing, vol. GE-21, pp. 118–121, 1983.

[4] Science Plan for the Alaska SAR Facility Program. Phase 1: Data from the First Remote Sensing Satellite, ERS-1, Jet Propulsion Laboratory Document JPL 89–14, Jet Propulsion Laboratory Publisher, Pasadena, CA, 1989.

[5] E. Attema, "The active microwave instrument on-board the ERS-1 satellite," Proc. IEEE, vol. 79, pp. 791-799, 1991

[6] D. Cuddy, M.J. Chen, and T. Bicknell, "Alaska SAR processor implementation for ERS-1," in Proc. Int. Geosci. Remote Sensing Symp. IGARSS'92, IEEE Cat. 92CH3041-1, Houston, TX, 1992, pp. 599-602.

[7] T. Bicknell, Alaska SAR Facility SAR Processor System: User's Guide to Products, JPL Document D-9362, Jet Propulsion Laboratory, Pasadena, CA, 1992.

[8] E. Attema, "Science requirements for the calibration of the ERS-1 Synthetic Aperture Radar," in Proc. CEOS SAR Calibration Workshop, Ottawa, Canada, Sept. 21-25, 1992.

[9] R. Fatland and A. Freeman, "Calibration and change detection of ASF/ERS-1 SAR image data," in Proc. Int. Geosci. Remote Sensing Symp. IGARSS'92, IEEE Cat. 92CH3041-1, Houston, TX, 1992, pp. 1164-1166.

[10] R. Touzi, A. Lopes, and P. Bousquet, "A statistical and geometrical edge detector for SAR images," IEEE Trans. Geosci. Remote Sensing, vol. GE-26, pp. 764-773, 1988.

[11] J. Villasenor, D. Fatland, and L. Hinzman, "Change detection on Alaska's north slope using repeat-pass ERS-1 SAR images," IEEE Trans. Geosci. Remore Sensing, vol. 31, no. 1, pp. 227–236, Jan. 1993.

[12] E. Rignot and R. Chellappa, "A Bayesian classifier for change detection," in Proc. Int. Conf. Acoust., Speech, Signal Processing ICASSP'92, IEEE Cat. 92CH3101-9, San Francisco, CA, vol. 3, 1992, pp. 25-28,

[13] J. J. van Zyl and J. C. Shi, "The effect of topography on SAR calibration," IEEE Trans. Geosci. Remote Sensing, to be published..

[14] E. Rignot and R. Chellappa, "Segmentation of synthetic aperture radar complex imagery," J. Opt. Soc. Amer., A, vol. 8, pp. 1499-1509, 1991.

[15] E. Jakeman and R. Tough, "Generalized K-distribution: A statistical model for weak scattering,"J. Opt. Soc. Amer., A, vol. 4, pp. 1764-1772, 1987.

[16] H. Zebker and J. Villasenor, "Decorrelation in interferometric radar echoes," IEEE Trans. Geosci. Remote Sensing, vol. 30, pp. 950-959, 1992.

[17] J. B. Way et al., "The effect of changing environmental conditions on microwave signatures of forest ecosystems: Preliminary results of the Mar. 1998 Alaskan aircraft SAR experiment," Int. J. Remote Sensing, vol. 11, pp. 1119-1144, 1990.

[18] E. Rignot, J. B. Way, K. McDonald, P. Adams, and L. Viereck, "Monitoring of environmental conditions in Alaskan forests using ERS-1 SAR," in Proc. Int. Geosci. Remote Sensing Symp. IGARSS'92, IEEE Cat. 92CH3041-1, Houston, TX, 1992, pp. 530–532.

[19] E. Rignot and J. B. Way, "Monitoring freeze-thaw along North-South Alaskan transect using ERS-1 SAR," Remote Sensing of Environ., submitted for publication, 1993.

Eric J. M. Rignot (M'81) was born in Chambon sur Lignon, France. He received the Engineer's diploma from the Ecole Centrale des Arts et Manufactures Paris in 1985, the M.S. degree in astronomy from the University of Paris VI in 1986, and the M.S. degrees in aerospace engineering and in electrical engineering in 1987 and 1988, respectively, and the Ph.D. degree in electrical engineering in 1991, from the University of Southern California.

He was employed as a Research Assistant at the University of Southern California in the Department of Aerospace Engineering in 1986–1988. He then joined the Radar Science and Engineering Section at the Jet Propulsion Laboratory, California Institute of Technology. He is a Principal Investigator and a Coinvestigator on the Greenland AIRSAR Experiment, and on ERS-1 SAR projects. His research interests include analysis of radar scattering from glacier facies, monitoring of environmental changes in boreal forests using ERS-1 SAR, retrieval of forest parameters from SAR data, and sea-ice classification from multiparameter SAR data.

Dr. Rignot is a member of AGU.

Jakob J. van Zyl (S'85–M'86) was born in Outjo, Namibia, in 1957. He received the Hons. B. Eng. degree cum laude in electronics engineering from the University of Stellenbosch, Stellenbosch, South Africa, in 1979, and the M.S. and Ph.D. degrees in electrical engineering from the California Institute of Technology, Pasadena, in 1983 and 1986, respectively.

In 1984 he was the recipient of a Schlumberger Foundation fellowship. He was a Teaching Assistant for a course on the physics of remote sensing at the California Institute of Technology from 1983 to 1986. At present he is the Technical Group Supervisor of the Aircraft SAR group in the Radar Science and Engineering Section and the Program Manager for the Airborne Active Microwave Instruments Program at the Jet Propulsion Laboratory, Pasadena, CA. His current interests include studying theoretical electromagnetic problems related to polarimetric scattering, remote sensing, and the analysis of polarimetric SAR data.

Dr. van Zyl is a five-year member of the Institute for Electromagnetics Modeling and Applications of the Electromagnetics Academy.